January 2017

# Nanostructures, concentrations and energies: an ideal equation to extend therapeutic efficiency on radioresistant 9L tumour cells using Ta2O5 ceramic nanostructured particles

Ryan Brown
*University of Wollongong*, rsb084@uowmail.edu.au

Stephanie Corde
*University of Wollongong*, scorde@uow.edu.au

Sianne Oktaria
*University of Wollongong*, so819@uowmail.edu.au

Konstantin K. Konstantinov
*University of Wollongong*, konstan@uow.edu.au

Anatoly B. Rosenfeld
*University of Wollongong*, anatoly@uow.edu.au

*See next page for additional authors*

# Nanostructures, concentrations and energies: an ideal equation to extend therapeutic efficiency on radioresistant 9L tumour cells using Ta2O5 ceramic nanostructured particles


## Abstract

This work presents an in-depth analysis into the dependencies of radiosensitisation on X-ray beam energy, particle morphology and particle concentration for $Ta_2O_5$ nanostructured particles. A maximum sensitisation enhancement ratio of 1.46 was attained with irradiation of a 10 MV x-ray photon beam on 9L cells exposed to the less aggregated form of NSPs at 500 $\mu g/mL^{-1}$. A significant increase in sensitisation of 30% was noted at 150 kVp for irradiation of the less aggregated form of tantalum pentoxide NSPs compared to its more agglomerated counterpart. Interestingly, no differences in sensitisation were observed between 50 and 500 $\mu g/mL^{-1}$ for all beam energies and NSPs tested. This is explained by a physical "shell effect", where by the NSPs form layers around the cells (observed using confocal microscopy), with the inner layers contributing to enhancement, while the outer layers shield the cell from damage.



## Keywords

9l, tumour, energies:, cells, concentrations, ta2o5, ceramic, nanostructured, radioresistant, particles, nanostructures, efficiency, therapeutic, extend, equation, ideal

## Disciplines

Medicine and Health Sciences

## Publication Details

Brown, R., Corde, S., Oktaria, S., Konstantinov, K., Rosenfeld, A., Lerch, M. & Tehei, M. (2017). Nanostructures, concentrations and energies: an ideal equation to extend therapeutic efficiency on radioresistant 9L tumour cells using Ta2O5 ceramic nanostructured particles. Biomedical Physics & Engineering Express, 3 (1), 015018-1-015018-13.



## Authors

Ryan Brown, Stephanie Corde, Sianne Oktaria, Konstantin K. Konstantinov, Anatoly B. Rosenfeld, Michael L. F Lerch, and Moeava Tehei

Nanostructures, concentrations and energies: an ideal equation to extend therapeutic efficiency on radioresistant 9L tumor cells using $Ta_2O_5$ ceramic nanostructured particles



2017 Biomed. Phys. Eng. Express 3 015018

(http://iopscience.iop.org/2057-1976/3/1/015018)

Biomedical Physics & Engineering Express

OPEN ACCESS

RECEIVED
28 May 2016

REVISED
29 December 2016

ACCEPTED FOR PUBLICATION
5 January 2017

PUBLISHED
30 January 2017



PAPER

# Nanostructures, concentrations and energies: an ideal equation to extend therapeutic efficiency on radioresistant 9L tumor cells using $Ta_2O_5$ ceramic nanostructured particles

**Ryan Brown[1,2], Stéphanie Corde[1,3], Sianne Oktaria[1,2,4], Konstantin Konstantinov[2,5], Anatoly Rosenfeld[1,2], Michael Lerch[1,2] and Moeava Tehei[1,2,4]**

[1] Centre for Medical Radiation Physics, University of Wollongong, NSW, Australia
[2] Illawarra Health and Medical Research Institute, University of Wollongong, NSW, Australia
[3] Radiation Oncology Department, Prince of Wales Hospital, Randwick, NSW, Australia
[4] Centre for Medical Bioscience, University of Wollongong, NSW, Australia
[5] Institute for Superconducting and Electronic Materials, University of Wollongong, NSW, Australia

**E-mail:** moeava@uow.edu.au

**Keywords:** tantalum pentoxide nanoparticles, high-*Z*, radiosensitiser, dose enhancement, radioresistant

## Abstract

This work presents an in-depth analysis into the dependencies of radiosensitisation on x-ray beam energy, particle morphology and particle concentration for $Ta_2O_5$ nanostructured particles (NSPs). A maximum sensitisation enhancement ratio of 1.46 was attained with irradiation of a 10 MV x-ray photon beam on 9L cells exposed to the less aggregated form of NSPs at 500 $\mu$g ml$^{-1}$. A significant increase in sensitisation of 30% was noted at 150 kVp for irradiation of the less aggregated form of tantalum pentoxide NSPs compared to its more agglomerated counterpart. Interestingly, no differences in sensitisation were observed between 50 and 500 $\mu$g ml$^{-1}$ for all beam energies and NSPs tested. This is explained by a physical 'shell effect', where by the NSPs form layers around the cells (observed using confocal microscopy), with the inner layers contributing to enhancement, while the outer layers shield the cell from damage.

Cancer represents one of the foremost incurable diseases of not only contemporary times, but also historically and for the foreseeable future. Currently, cancerous disease accounts for 1 in 8 deaths worldwide [1] with over 50% of patients [2] utilising some form of radiotherapy in their treatment plan. This method relies on x-rays irradiating the target volume, however, it is difficult to maximise damage to the tumor volume, increasing tumor control probability, while sparing healthy tissue. One potential solution is based on artificially increasing local energy deposition to the tumor itself, effectively sparing surrounding non-cancerous tissue. Known as dose enhancement radiotherapy (DERT), this technique involves the introduction of high-*Z* atoms into close proximity to the tumor which, following exposure from the local radiation field, increases the selective damage and killing of the tumor cells. This radiation-induced increase in radiosensitivity is facilitated by the production of charged particles and reactive oxygen species (ROS), which are created when incoming photons interact with target high-*Z* atoms. The use of high-*Z* atoms are favorable due to the increased probability of photon interactions, which stems from the *Z*-dependence of the mass attenuation coefficient. The mass attenuation coefficient due to the photoelectric effect $\left(\frac{\tau}{\rho}\right)$ is approximately proportional to $\left(\frac{Z}{E}\right)^3$, where $Z$ is the atomic number of the absorbing medium and $E$ is the energy of the incident photon. Furthermore, the mass attenuation coefficient due to pair production $\left(\frac{\kappa}{\rho}\right)$ exhibits a $Z^2$ dependence [3]. DERT is especially promising for the treatment of aggressive radioresistant tumors and tumor cells, such as gliomas, which have been known to exhibit radioresistance in the form of hypoxia and are surrounded by critical structures [4]. This makes localised dose enhancement particularly beneficial in successfully achieving local tumor control without significantly increasing the dose to surrounding normal tissues. The gliosarcoma 9L cell line has been utilised in this study as it represents a well-

characterised radioresistant cell line and animal tumor model for human gliomas [5].

The main interactions of concern between the incoming photon x-ray beam and the target nanostructured particles (NSPs) leading to dose enhancement include: the photoelectric effect, Compton scattering and pair production, with the dominant process dependent on the incident beam energy. At 10 MeV energies, the photoelectric effect is less likely than the other processes, only occurring approximately 18% of the time [6]. The secondary electrons produced are consequently high energy in nature, with low linear energy transfer (LET). LET is a measure of the average energy deposited locally to the absorbing medium per unit length $\left(\frac{dE}{dx}\right)$ for a charged particle along its track [7], and is particularly important to consider for this study as particles with high LET provide desirable increases in the relative biological effectiveness (RBE) of the local radiation environment. At keV energies, the photoelectric effect is the dominating interaction process, with the highest cross-sectional probability, and not only results in the production of photoelectrons, but can also lead to Auger cascades. These Auger electrons have an LET of 10–25 keV $\mu m^{-1}$ [8], representing high LET particles, which are particularly desirable in DERT applications. In the context of this study, short range particles such as these will be unable to penetrate NSP aggregates, and will only contribute to dose enhancement if produced in close proximity to the cell, unimpeded by any aggregates. Compton scattering is significant at both MeV and keV energies, however because this process has no $Z$-dependence it does not largely contribute to high-$Z$ enhancement. Because pair production has a minimum threshold photon energy of 1.022 MeV, the process is non-existent at keV energies, and has a cross section that increases with energy above the threshold. The dominance of this process at MeV energies means the secondary electrons produced are high energy in nature, therefore having low LET of approximately 0.2 keV $\mu m^{-1}$ for kinetic energies of 1–10 MeV [9]. Consequently, the high range of these secondary electrons means they are able to penetrate several micron-thick layers of NSP aggregates before damaging the cell. High-$Z$ materials used in DERT have been dominated by metal nanoparticles (NPs) in the form of gold, platinum and gadolinium. Au NPs have emerged as a leading contender in the field, with initial *in vivo* studies by Hainfeld *et al* revealing dose enhancement ratios (DERs) up to 6 using 1.9 nm Au NP concentrations of 7 mg $g^{-1}$ (Au to tumor mass ratio) and 250 kVp irradiation on mice containing subcutaneous EMT-6 mammary carcinomas [10]. Although popularity for research has revolved around kilovoltage (kVp) energy x-rays, recent studies by Jain *et al* have generated sensitisation enhancement ratios (SERs) of 1.29 and 1.16 on MDA-MB-231 cells treated with 12 $\mu$M 1.9 nm Au NPs using 6 megavoltage (MV) and 15 MV x-ray beams, respectively [11].

Ceramic NPs are now emerging as potential alternatives to metal NPs in DERT. Initially, ceramic NPs in the form of $CeO_2$ were used as radioprotectors [12], however, it has recently been shown that the influence of the high-$Z$ component at kVp energies creates a dose enhancement effect, when sensitisation outweighs the protective free radical scavenging effect [13]. Following this, we revealed $Ta_2O_5$ NSPs as the first nanoceramics to provide effective radiosensitisation of radioresistant tumor cells. In this recent study, $Ta_2O_5$ NSPs were shown to be non-toxic to 9L cells and yielded an SER of 1.33 with a 10 MV x-ray beam [14]. We postulate that this effective enhancement at MV energies could be attributed to secondary electrons produced through photoelectric interactions and pair production, with scattering on NSP aggregates leading to increased radiobiological effectiveness. We expect that these NSP aggregates will be less effective at kVp energies due to the absorption of the short range secondary electrons produced by the comparatively larger aggregates. Higher concentrations are also predicted to be less effective owing to the increase in aggregation and, therefore aggregate size associated with higher concentrations of NPs. To investigate this hypothesis, two morphologically different phases of $Ta_2O_5$ NSPs were prepared by thermal oxidation—referred to as thermal nanostructured particles (TNSPs)—and precipitation—referred to as precipitation nanostructured particles (PNSPs)—reactions. Experiments were performed at kVp energies, as well as MV energies, at different concentrations utilising the original aggregative $Ta_2O_5$ NSP (TNSP), as well as a new $Ta_2O_5$ NSP with reduced tendency for aggregation (PNSP). The biological and physical mechanisms underlying changes in these factors were additionally examined, with respect to their effect on radiosensitisation.

This work presents an in-depth analysis into the dependencies of radiosensitisation on beam energy, particle morphology and particle concentration for $Ta_2O_5$ NSPs. The 9L gliosarcoma rat-brain cell line was chosen for all experiments due to its known radioresistant characteristics, and the fact that it is a well-researched [15] and well-characterised animal tumor model [5, 16]. Bencokova *et al* [17] proposed that *in vitro* 9L cells were radioresistant due to their fast DNA repair mechanisms, including efficient repair of lethal double-strand breaks (DSBs). They also reported that 9L was more radioresistant than other rat tumor models, including C6 and F98 cell lines. Analysis of multiple beam energies is essential with MV energies signifying not only the majority of beam treatments, but also the most relevant area of the energy spectrum to treat the majority of cancers. The kVp range is of particular interest, since this represents the most intensely researched energy in DERT and leads to the production of high LET electrons creating

more damage. The 150 kVp beam was chosen for both its clinical relevance and to maximise the dose enhancement to the NSP doped medium relative to a water equivalent medium, based on the formalism described by Corde *et al* [18]. This formalism uses the ratio of the mass attenuation coefficient for $Ta_2O_5$ to water, as a function of photon energy, to predict the optimal energy for maximising photon interactions and, therefore, dose enhancement [18] in a water-based medium. The 150 kVp beam produces an effective energy of 65 keV, based on half-value layer beam quality measurements [19] used to characterise the beam for experimentation at POWH, which lies close to, yet above the effective energy required to maximise dose enhancement in $Ta_2O_5$ (33 keV). Investigation into kVp energies also lays the foundations for future experimentation with emerging cancer treatment modalities using synchrotron radiation. The synchrotron allows for the production of a monochromatic keV radiation beam accurately tuned to the optimal energy for absorption in the material with high dose rate, having the potential to drastically increase radiosensitisation. Additionally, investigation into the effect of increasing NP concentration on SER is again important, since it is widely thought that this relationship should increase the SER, however Butterworth *et al* has shown that depending on the cell line, increasing the concentration of the NP may increase, decrease or, in fact, not change the SER [20], although no mechanism for explaining this effect was suggested.

## Methods

### NSP production and preparation

Tantalum pentoxide TNSPs were synthesised using a thermal oxidation reaction. This process involved solid state thermal oxidation of Ta metal foil with purity 99.99%. The foil was placed in an alumina crucible prior to heating at 800 °C for 1 h, which leads to complete oxidation and formation of $Ta_2O_5$ nano powder.

Tantalum pentoxide PNSPs were synthesised using a precipitation-based chemical reaction utilising $Ta(OEt)_5$ (Sigma-Alrich 99.99%) and an ethoxide decomposition reaction with water. This method was derived from the article written by Kominami *et al* [21]. Two drops (1 ml) of $Ta(OEt)_5$ was first added to a small amount of ethanol (15 ml) and mixed carefully to avoid disrupting the surface of the ethanol. Excess deionised water was added resulting in a white fine precipitate that was filtered out and washed, using a centrifuge (Eppendorf model 5702). The filtered tantalum hydroxide powder was placed in a furnace and heated for 8 h at 700 °C, where by thermal decomposition occurs and $Ta_2O_5$ nanocrystallites form. Drying of the resultant NSPs was necessary to avoid violent agglomeration. This was achieved by placing them on an aluminum crucible inside a furnace at 140 °C for a minimum of 2 h. Finally, sterilisation inside an autoclave at 121 °C for 45 min ensured the elimination of any contaminants that could jeopardise cell culture experiments. The NSPs were suspended in phosphate buffered saline (PBS) (without calcium and magnesium ions) to ensure homogeneity in concentration before being applied to the cells. Furthermore, sonication of the NSP solution was employed to reduce the degree of aggregation and create a more even distribution of the NSPs in solution. A 15 ml falcon tube containing the solution was sonicated with a fine tip probe in an ultrasonic bath environment for 30 min total in 10 min intervals.

### Cell line and culture

Cellular experiments employed a culture of 9L gliosarcoma cancer cells derived from rodent brain cells [16]. The cells were maintained in a T75 $cm^2$ flask with complete Dulbecco's Modified Eagle Medium (c-DMEM from GIBCO, supplemented with 10% fetal bovine serum and 1% Penicillin and Streptomycin) and incubated at 37 °C and 5% (v/v) $CO_2$.

### X-ray diffraction (XRD)

Characterisation of the NSP involved the use of XRD for determination of phase, structure, particle size and unit cell parameters. A sample of tantalum pentoxide NPs was placed in a GBC MMA XRD system (GBC Scientific Equipment Pty Ltd, Victoria, Australia) using Cu *K*-alpha radiation with wavelength $\lambda = 1.5418$ Å, accelerating voltage 40 kVp and cathode current 30 mA, in order to determine information regarding crystal structure and mean particle size ($t$). Mean crystallite size ($t$) was determined through utilisation of Scherrer's equation [22].

### High resolution-transmission electron microscopy (HRTEM)

Morphological parameters—crystallinity, size, agglomeration and shape—were investigated using a 200 kVp (HRTEM, JEOL, 2011, USA).

### Flow cytometry analysis

9L cells were exposed to $Ta_2O_5$ TNSPs and PNSPs at concentrations of 0, 50 and 500 $\mu g\,ml^{-1}$ for 24 h. Trypsinisation was used to detach the 9L cells before being placed in a centrifuge at 1500 rpm and 4 °C for 5 min and rinsing twice with cold PBS (without calcium and magnesium). Flow cytometric measurements and analyses were performed using a Becton-Dickinson fluoresence-activated cell sorting (FACS) flow cytometer (BD LSR II; BD Biosciences, Franklin Lakes, USA). Each analyzed sample contained a minimum of 10 000 cells where cell doublets and aggregates were gated out using a two parameter histogram of FL2-Area versus FL2-Height. Data analysis was performed using the FACSDiva software, assessing both forward (FSC) and side scatter (SSC)

intensities. The median cell SSC values were employed as a marker of cellular granularity, which is proportional to particle uptake and internalisation [23].

**Clonogenic cell survival assay**

Clonogenic assays were used to assess cell survival. Cells were plated in triplicate for: a control (no NSP), 50 $\mu$g ml$^{-1}$ and 500 $\mu$g ml$^{-1}$ concentration of tantalum pentoxide NSPs. The 9L cells were brought to 90% confluence, tantalum pentoxide NSP solution prepared and added to the cell culture medium; then once exposure time had been reached the cells were split into 100 mm petri dishes with 10 ml c-DMEM and incubated for 21 days, equivalent to 15 doubling times. Following this, each dish was washed with 5 ml PBS (with calcium and magnesium ions) and stained with 5 ml of staining solution (25% crystal violet and 75% ethanol). Colonies were counted and considered viable if they consisted of approximately 50 cells or more ($n$), and compared with inital seeding values ($I$) to obtain the plating efficiency (PE).

$$\mathrm{PE} = \frac{n}{I}. \tag{1}$$

The surviving fraction (SF) could then be determined by comparing the control PE ($\mathrm{PE_c}$) with the PE of the group containing the NSP ($\mathrm{PE}_x$).

$$\mathrm{SF} = \frac{\mathrm{PE}_x}{\mathrm{PE_c}}. \tag{2}$$

**Toxicity assessment**

To assess the toxicity of TNSPs and PNSPs to 9L cells, NSP concentrations of 0 (2 controls), 50, 100, 200 and 500 $\mu$g ml$^{-1}$ were exposed to 9L cells for a period of 24 h prior to plating. 9L cells were brought to 90 % confluence inside T12.5 cm$^2$ flasks (BD Falcon$^{\mathrm{TM}}$) before exposure to the NSP. Solutions of TNSPs and PNSPs were prepared according to the 'NSP Preparation' protocol, and the appropriate volumes corresponding to each concentration added to the cells. Once the desired exposure time had been reached, cells were plated in triplicate according to the 'clonogenic cell survival assay' technique. Following plate staining and colony counting, SFs were obtained for each NSP at each concentration, and normalised to the control group (0 $\mu$g ml$^{-1}$).

**Cellular irradiation with NSPs**

All radiation experiments were carried out at the radiation oncology department at the Prince of Wales Hospital (Randwick, NSW, Australia). Beam energies of 10 MV and 150 kVp were investigated using an Elekta Axesse$^{\mathrm{TM}}$ LINAC (Elekta AB, Kungstensgatan, Stockholm, Sweden) and a Nucletron Oldelft Therapax DXT 300 Series 3 Orthovoltage unit (Nucletron B.V., Veenendaal, The Netherlands), respectively. The 9L cell culture was exposed to the tantalum pentoxide NSPs for 24 h at concentrations of 50 and 500 $\mu$g ml$^{-1}$. For MV experiments, 9L cells were irradiated in T12.5 cm$^2$ flasks (BD Falcon$^{\mathrm{TM}}$) completely filled with Hank's balanced salt solution so no air bubbles were present inside the flask to ensure electronic equilibrium conditions were present at the depth of the cells. For kVp experiments, cells were contained and irradiated in 6 mm of medium to maximise the accuracy in delivering the prescribed dose to the cell monolayer. All doses (1, 2, 3, 5 and 8 Gy) were delivered in single fractions at room temperature with dose rates of 5 and 0.7 Gy min$^{-1}$ for 10 MV and 150 kVp x-ray photon beam energies, respectively. Tissue culture flasks were irradiated horizontally surrounded by a 30 × 30 × 10 cm$^3$ solid water phantom to ensure backscattering effects were taken into account and human physiological conditions accurately modeled, with the cell monolayer situated at an SSD of 100 cm and 50 cm for 10 MV and 150 kVp beam energies, respectively. Unirradiated control samples (with and without tantalum pentoxide NSPs) were utilised and handled under the same conditions as the irradiated samples.

It is worth noting here that although different dose rates have been utilised at each energy, the dose rate effect has been tested on 9L cells at the dose rates utilised in this study and revealed an insignificant effect on the survival of 9L cells [24].

**Cell survival analysis**

Survival curves were fit according to the linear quadratic model (LQM) using the associated error bars of each point as weighting factors. The error bars for each point represent 1 standard deviation from the mean. The LQM [25] describes cell SF mathematically as a function of absorbed dose ($D$).

$$\mathrm{SF}(D) = \mathrm{e}^{-\alpha D - \beta D^2}. \tag{3}$$

The parameters $\alpha$ (Gy$^{-1}$) and $\beta$ (Gy$^{-2}$) are indicative of cell radiosensitivity and repair effectiveness respectively. We were able to extrapolate these values based on the fit for each survival curve and compare experiments (with and without the NSP) to quantify the degree of dose enhancement by calculation of the SER (the ratio of doses giving 10% SF on the cell survival curves).

**Sensitisation enhancement ratio**

We measured the degree of dose enhancement by means of the SER, defined as the ratio of doses giving 10% SF on the cell survival curves. Given dose ($D$) as a function of SF on two curves, namely the control curve with no NSP ($D_{\mathrm{c}}$(SF)) and the curve containing the NSP ($D_x$(SF)), the SER can be mathematically expressed as:

$$\mathrm{SER} = \frac{D_{\mathrm{c}}(0.1)}{D_x(0.1)}. \tag{4}$$

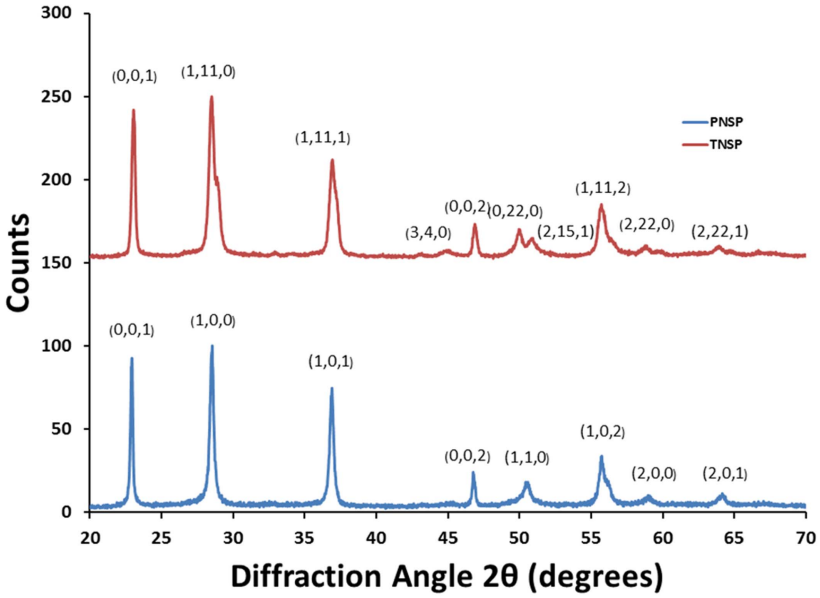


**Figure 1.** XRD patterns illustrating various peaks of reflection, and their corresponding Miller indices, for TNSPs and PNSPs.

**Table 1.** Mean crystallite size, unit cell parameters, crystal structure and phase summarised for the TNSPs and PNSPs.

| Type of $Ta_2O_5$ | Size (nm) | $a$ (Å) | $b$ (Å) | $c$ (Å) | Structure | Phase |
|---|---|---|---|---|---|---|
| TNSP | 56 | 6.2 | 40.29 | 3.89 | Orthorhombic | Beta |
| PNSP | 45.5 | 3.62 | 3.62 | 3.88 | Hexagonal | Delta |

### Confocal microscopy

Light and fluorescence microscopy images were obtained using a Leica confocal laser scanning microscope (Leica TCS SP5 Advcanced System UVVIS-IR and X1-Port Access with SMD FCS and $CO_2$ incubation chamber, Germany) and the accompanying image manager software Leica Application Suite Advanced Fluorescence (LAS AF, v.2.6.17314, Germany) located at the Illawarra Health and Medical Research Institute (IHMRI), Wollongong, Australia.

### Statistical analysis

Cell survival experiments were repeated to ensure reliability and measured in triplicate for each sample. All values are expressed as the mean of three measurements with the experimental uncertainty given as one standard deviation. The LQM model was fitted to cell survival data using KaleidaGraph software. The fit of the data was weighted according to the error for each dose in the determination of the radiobiological constants, $\alpha$ and $\beta$. Statistical analysis of SF data was performed using a two-tailed Student's t-test under the assumption of equal variance. A $P$ value less than, or equal to 0.05 was considered statistically significant.

## Results

### Characterisation of NSP crystal structure

Diffraction patterns were constructed for each NSP, shown in figure 1, with each curve containing peaks of similar shape, intensity and position, indicative that the NSP samples are of similar atomic composition, namely $Ta_2O_5$. Closer inspection of the TNSP pattern revealed the existence of additional smaller peaks, compared to the PNSP pattern, signifying a structural difference between the samples despite their similar chemical composition. Peak analysis and database comparison of the diffraction patterns revealed the TNSPs to be orthorhombic beta phase (JCPDS:25-0922), while the PNSPs are hexagonal delta phase (JCPDS:19-1299). This structural difference is fundamentally linked to the production methods employed for each NSP, where by the annealing temperature of 700 °C produces hexagonal phase $Ta_2O_5$ for the PNSPs, as opposed to 800 °C for the TNSPs, which results in orthorhombic formation. This is supported in the literature, where the temperature threshold for orthorhombic transformation in $Ta_2O_5$ NPs has been shown to be 750 °C [26]. The most notable feature of this transformation is the splitting of (1,1,0) hexagonal phase peak into (0,22,0) and (2,15,1) orthorhombic phase peaks [27], clearly evidenced in figure 1.

Additionally, the unit cell parameters were derived for each sample (data summarised in table 1) with

**Table 2.** Alpha, beta and SER for the TNSPs and PNSPs at 0, 50 and 500 $\mu$g ml$^{-1}$, as well as 150 kVp and 10 MV. Errors are given $\pm 1$ standard deviation from the mean.

| Beam energy and type of $Ta_2O_5$ | NSP concentration ($\mu$ g ml$^{-1}$) | $\alpha$(Gy$^{-1}$) | $\beta$(Gy$^{-2}$) | $SER_0$, $SER_{50}$, $SER_{500}$ |
|---|---|---|---|---|
| 150 kVp TNSP | 0 | 0.30 ± 0.04 | N/A | 1 |
| | 50 | 0.32 ± 0.05 | N/A | 1.07 ± 0.03 |
| | 500 | 0.33 ± 0.02 | N/A | 1.10 ± 0.07 |
| 150 kVp PNSP | 0 | 0.30 ± 0.04 | N/A | 1 |
| | 50 | 0.40 ± 0.01 | N/A | 1.33 ± 0.07 |
| | 500 | 0.43 ± 0.01 | N/A | 1.43 ± 0.08 |
| 10 MV TNSP | 0 | 0.19 ± 0.05 | 0.012 ± 0.008 | 1 |
| | 50 | 0.38 ± 0.03 | N/A | 1.33 ± 0.07 |
| | 500 | 0.40 ± 0.03 | N/A | 1.40 ± 0.07 |
| 10 MV PNSP | 0 | 0.19 ± 0.05 | 0.012 ± 0.008 | 1 |
| | 50 | 0.39 ± 0.03 | N/A | 1.36 ± 0.07 |
| | 500 | 0.43 ± 0.03 | N/A | 1.46 ± 0.07 |

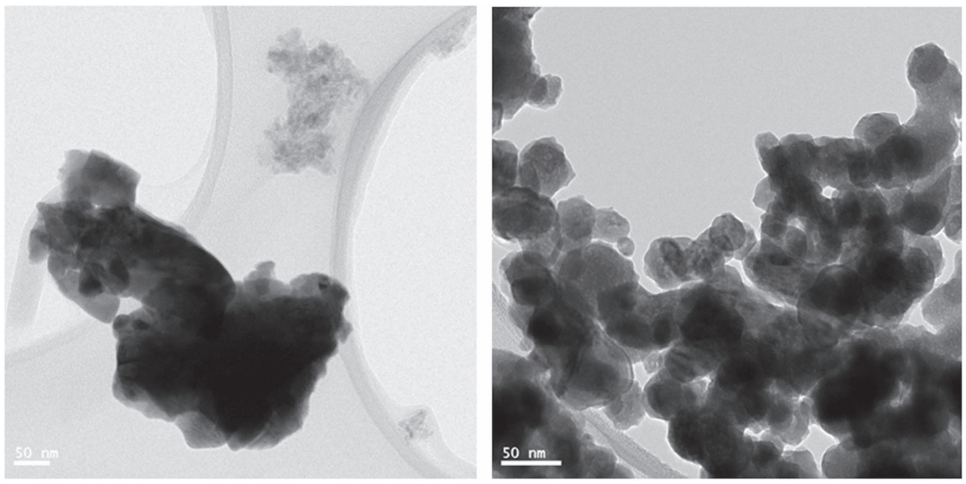


**Figure 2.** HRTEM images of the TNSPs (left) and PNSPs (right) captured at a scale of 50 nm.

$a = b$ characteristic of the hexagonal structure in the PNSPs [28]. Mean crystallite size ($t$) was calculated by means of Scherrer's equation [22] and analyis of an appropriate peak (0,0,1), proving the TNSPs (56 nm) to be larger than the PNSPs (45.5 nm). With regards to DERT, these sizes are quite large compared to Au NPs, which commonly employ 1.9 nm [20] and even 1.4 nm [29], suggesting their ability to be internalised by cells may be undermined. However, a study into NP size-dependency of internalisation has revealed 50 nm to be the optimal size for internalisation of Au NPs [30], suggesting damage to cells will be maximised and validating our choice to investigate NSPs of this size.

### NSP morphological characterisation

High quality images acquired (figure 2) indicated that both NSPs are highly crystalline in nature, possessing mean crystallite sizes in agreement with that derived using Scherrer's formula. The tendency for agglomeration is seen to differ significantly between the two samples, with the TNSPs exhibiting larger aggregates approximately 400 $\mu$m in maximum size, while the PNSPs are globally much more dispersed with maximum aggregates of 100 $\mu$m. It must be noted that the sample preparation process causes the NSPs to agglomerate, so that the actual aggregate size in solution is much less. This difference in particle aggregation may be attributed to their respective production methods, where by the higher reaction temperature in thermal decomposition of the TNSP results in larger crystallites, with increased size distribution, and larger aggregates. Comparatively, the precipitation reaction utilises a lower reaction temperature, and involves dispersion treatment so that the crystallites are less likely to aggregate in an attempt to reduce the total surface energy of the material. These differences in the methods of synthesis directly affect the NSP (crystallite) morphology, there by influencing aggregate morphology as well. The TNSPs consist of larger crystallites, higher in aspect ratio, irregular in shape and less dispersed leading to aggregates which are larger and less dispersed than their PNSP counterparts.

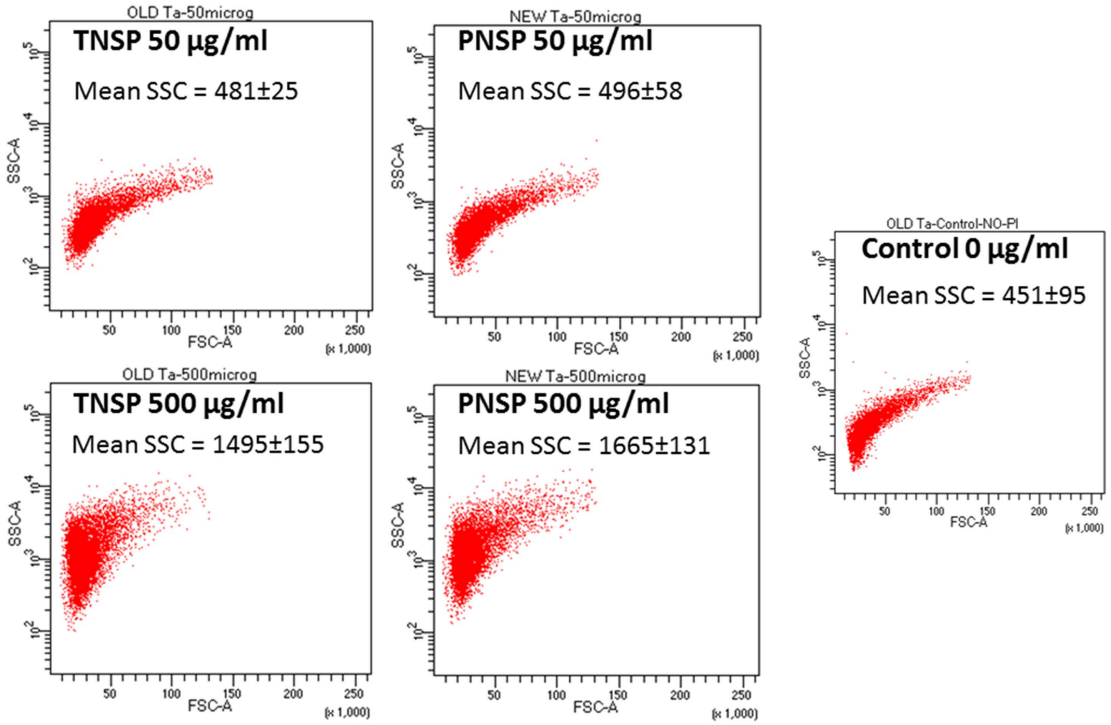


**Figure 3.** FSC versus SSC histograms representative of 9L cellular uptake of TNSPs and PNSPs at 0, 50 and 500 $\mu$g ml$^{-1}$ following 24 hours exposure.

The two NSPs are also morphologically dissimilar in terms of shape. The TNSPs display an irregular shape while the PNSPs are distinctly spherical. Based on the smaller crystallite size and resistance to aggregation, we would naturally expect the PNSPs to be more easily internalised than the TNSPs. The less obvious fact, though, is that the spherical nature of the PNSPs also increases their degree of internalisation. It has been shown for Au that spherical NPs portray preferential uptake to other shapes, such as nanorods, in HeLa cells. In this particular study, endocytosis was identified as the mechanism of internalisation, with low aspect ratio spherical NPs being preferentially internalised due to greater availability of cell receptor bonding sites for serum proteins, which initiate endocytosis [30]. Evidently, we not only expect the PNSPs to be more easily internalised than their thermal counterparts, there by imparting greater damage to the cells, but we may also expect the internalisation mechanism to be endocytosis. This is confirmed with the results presented in the FACS flow cytometry and confocal microscopy sections.

### Flow cytometric analysis of NSP uptake in 9L cells

The magnitude of forward (FSC) and side (SSC) scatter are representative of cell diameter (size) and granularity respectively, with changes in cellular granularity (mean SSC) proportional to the degree of internalisation [31]. Data was presented in the form of a histogram with SSC graphed as a function of FSC abscissa (figure 3).

For all concentrations tested, we see no significant difference in the mean SSC values when comparing the two NSPs themselves [23], suggesting both NSPs are internalised to a similar degree. When examining each NSP on its own and comparing to the control, we see significant increases in the degree of internalisation as the concentration of the NSP increases. Although this dependency has been rarely tested explicitly, it is not unheard of, with bismuth ferrite ($BiFeO_3$) NPs [31] and superparamagnetic iron oxide NPs [32] exhibiting similar trends. For both NSPs, we see an approximate 10% increase in the mean SSC values at 50 $\mu$g ml, and at 500 $\mu$g ml$^{-1}$ we observe a substantial increase in the mean SSC of approximately 300%. These results suggest that at low concentrations the majority of the NSPs remain external to the cell membrane as aggregates, while at higher concentrations a greater portion of the NSPs are internalised by the 9L cells.

### Toxicity of NSPs to 9L cells

Maximum toxicity values of approximately 20% and 30% were measured (figure 4) for TNSPs and PNSPs respectively. Significant drops in cell colonies and saturation occured at 100 $\mu$g ml$^{-1}$ for both NSPs. Additionally, both NSPs exhibited 80% SF at 100 $\mu$g ml$^{-1}$, which is exactly the same SF as 1.9 nm Au NPs tested at the same concentration on MDA-231-MB (breast cancer) cells (more sensitive than 9L) [20]. This suggests they are, at a minimum, comparable to Au NPs in terms of cytotoxicity, which are already used clinically in DERT and widely considered

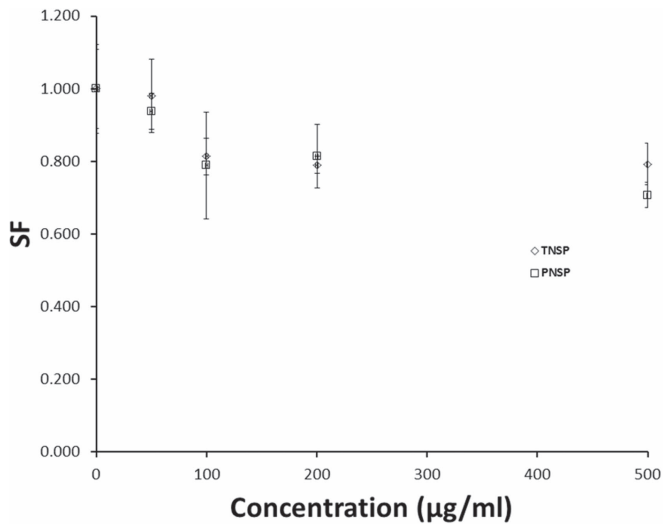


**Figure 4.** Cytotoxicity of TNSPs and PNSPs to 9L cells following a 24 hour period of exposure.

non-toxic [33]. Moreover, there is considerable support in the literature to suggest toxicity values as high as 50% may be considered non-toxic [34], supporting the fact that both tantalum pentoxide NSPs may be considered relatively non-toxic at the highest concentrations tested. These results formed the basis for the concentrations utilised in radiation experiments.

### The dependency of radiosensitisation on particle morphology, NSP concentration and beam energy for TNSPs and PNSPs on 9L cells in x-ray fields

Radiation experiments were performed using the clonogenic assay technique to assess the influence of particle morphology, NSP concentration and beam energy on sensitisation of 9L cells by TNSPs and PNSPs, with resultant survival curves (figure 5) fit according to the LQM.

Alpha and beta parameters were extrapolated based on SF data, and SERs calculated based on comparison of 10% survival doses (table Table 2). In all cases, cells containing either of the NSPs demonstrated lower SFs in comparison to the control, indicative of greater induced damage to the cells. Comparing results for each NSP, we see the PNSP exhibits significant sensitisation, far greater than that of the TNSP, for irradiation at 150 kVp and both concentrations examined (50 $\mu$g ml$^{-1}$, $p = 0.0274$ and 500 $\mu$g ml$^{-1}$, $p = 0.0126$), suggesting a morphological difference in the PNSPs gives them superior sensitisation ability at kVp beam energies. Similarly, we observe greater sensitisation by the PNSP at 10 MV for both concentrations tested, however the difference in SERs between the two NSPs proves to be statistically insignificant (50 $\mu$g ml$^{-1}$, $p = 0.6274$ and 500 $\mu$g ml$^{-1}$, $p = 0.3531$). At 10 MV, the effects of differing morphology, attributed to the TNSPs and PNSPs, on cell damage become less pronounced due to the long range (centimetres) of secondary Compton scattered electrons, as well as electrons and positrons originating from pair production, that are produced. These long range, low LET (0.2 keV $\mu$m$^{-1}$) particles produce uniform dose enhancement across the cell culture independent of NSP distribution, but rather dependent on the total NSP concentration.

Analyzing the effect of NSP concentration on sensitisation, we see insignificant increases in the SERs for the TNSP of approximately 3% at both beam energies tested (150 kVp, $p = 0.5655$ and 10 MV, $p = 0.2879$). The PNSP exhibits a slightly higher increase of 8% at both beam energies used (150 kVp, $p = 0.2017$ and 10 MV, $p = 0.1551$).

Finally, we observe significant beam energy dependence of sensitisation for the TNSPs, with approximate 25% increases in cell death from 150 kVp to 10 MV at both concentrations tested (50 $\mu$g ml$^{-1}$, $p = 0.0274$ and 500 $\mu$g ml$^{-1}$, $p = 0.063$). In contrast, the PNSPs exhibit a weaker dependence with an approximate increase of 3% from 150 kVp to 10 MV at both concentrations tested (50 $\mu$g ml$^{-1}$, $p = 0.6274$ and 500 $\mu$g ml$^{-1}$, $p = 0.6585$). This again supports our hypothesis that morphological differences in the two NSPs give rise to varying degrees of sensitisation for any given beam energy and concentration. Evidently, the results imply that the PNSPs are superior radiosensitisers to their TNSP counterparts, not only in terms of the magnitude of sensitisation, but also in consistency of delivering effective radiosensitisation across varying beam energies and nanocrystallite concentrations.

### Interaction of NSPs with 9L cells

Confocal microscope images were captured detailing the interaction of the TNSPs and PNSPs with 9L cells at concentrations of 0 (control), 50 and 500 $\mu$g ml$^{-1}$.

Analysis of the resultant images (figure 6) revealed that both NSPs show a specificity to the 9L cells at all

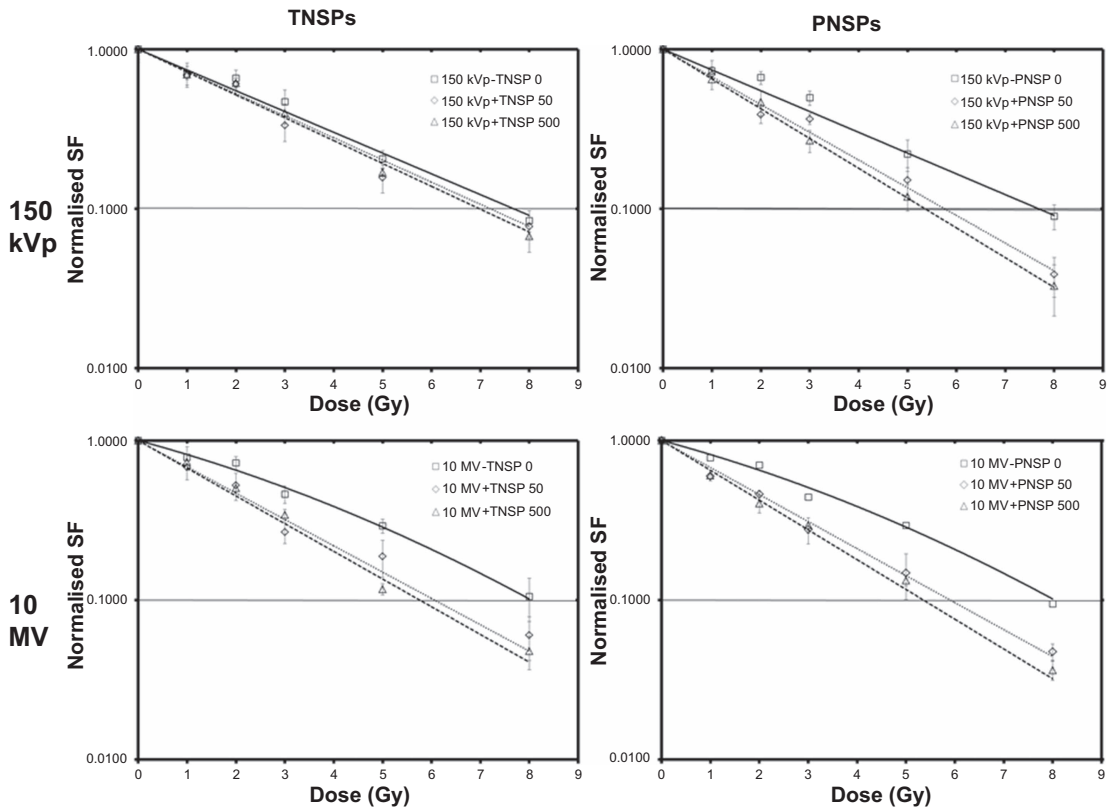


**Figure 5.** Cell survival curves for 9L cell cultures irradiated with 10 MV and 150 kVp x-rays showing the dose modifying response of tantalum pentoxide NSPs at concentrations of 50 and 500 $\mu$g ml$^{-1}$.

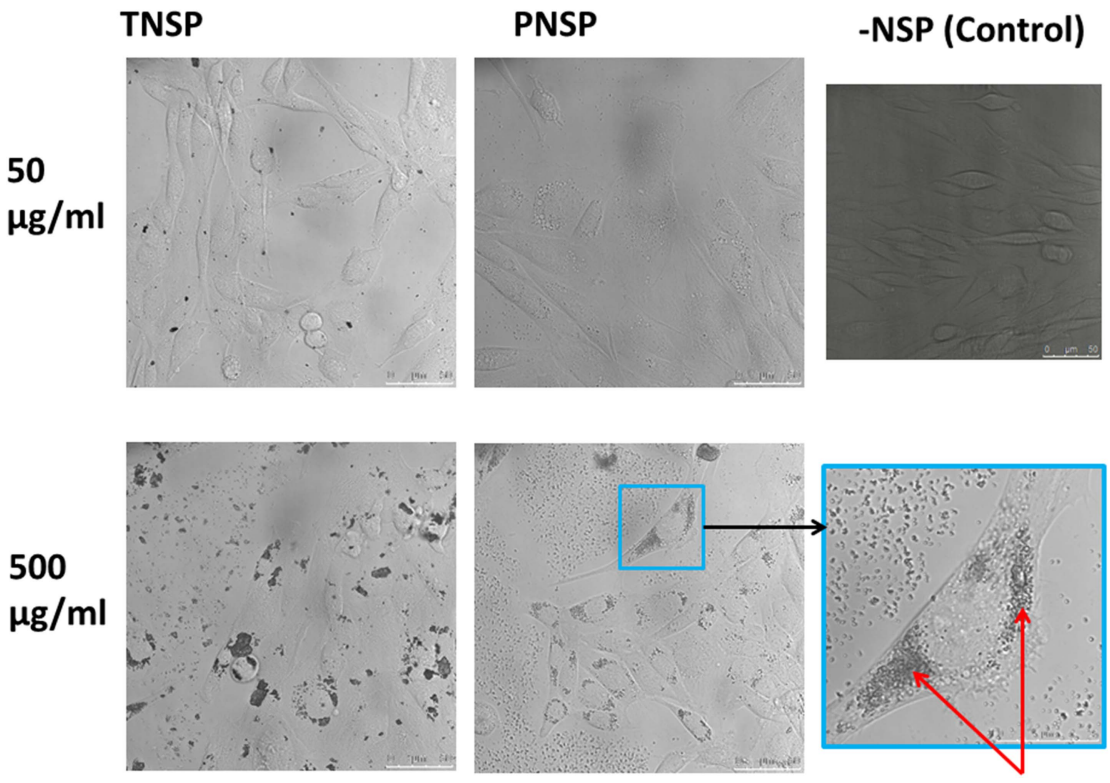


**Figure 6.** 9L cells treated with TNSPs (left column) and PNSPs (middle column) at concentrations of 50 and 500 $\mu$g ml$^{-1}$. The untreated sample is represented in the top right hand column, and the bottom right hand panel is a zoomed region from the adjacent panel containing 9L cells treated with PNSPs at 500 $\mu$g ml$^{-1}$. The red arrows indicate endosome-encapsulated PNSPs around the nucleus of the cell.

concentrations, forming aggregates and being attracted to the cellular membrane. This aggregation of the NSPs is more pronounced at the highest concentration tested (500 $\mu$g ml$^{-1}$). Comparing the two NSPs, we see the TNSPs are more prone to aggregation, forming much larger clusters around the 9L cells compared to the PNSPs, for all particle concentrations. On the other hand, the PNSPs show little to no aggregation and are of uniform size. Despite the lack of aggregation, clustering of the PNSPs is still observed around the cellular membrane and nucleus due to an intrinsic attraction of the PNSPs to the 9L cells. We also observe the presence of endosome-encapsulated NSPs (indicated by red arrows in figure 6), particularly in the 500 $\mu$g ml$^{-1}$ cases, suggesting the internalisation mechanism activated here is endocytosis. This is similar to Au NPs, which have been shown to exhibit clustering inside the cytoplasm of HeLa cells, and through the use of confocal imaging, were observed to localise in lysosomes [35]. Evidently, the images suggest the PNSPs are again superior to the TNSPs in terms of particle morphology (aggregation), specificity and internalisation. However, based on the significant increase in specificity and clustering from 50 to 500 $\mu$g ml$^{-1}$ for both NSPs, it would be logical to expect greater enhancement than what was observed in radiation experiments, although an explanation for this phenomenon is offered and supported by the results presented.

## Discussion

Significant radiosensitisation was observed in the majority of radiation experiments indicated by increased cell death of treated cells compared to their respective untreated control cells, with the exception of 150 kVp irradiation of TNSPs on 9L cells. A lack of enhancement is observed at this beam energy ($SER_{50} = 1.07$, $p = 0.0561$ and $SER_{500} = 1.10$, $p = 0.1318$) due to the existence of large TNSP aggregates, shown to be as large as 400 $\mu$m through HR-TEM imaging. At 150 kVp, the photoelectric effect and Compton scattering will dominate the majority of photon beam interactions, producing photoelectrons, Auger cascades and Compton scattered electrons. The average energy of these photoelectrons, as well as the Compton scattered electrons, is of the order of 50 keV or less, giving them a maximum range of 10 $\mu$m. On the other hand, the average energy of Auger electrons is much less, in the order of 10 eV, making them very high LET particles with a much smaller range of a few nanometers [36].

In contrast, irradiation of PNSPs on 9L cells at the same beam energy (150 kVp) reveals significant sensitisation ($SER_{50} = 1.33$, $p = 0.0147$ and $SER_{500} = 1.43$, $p = 0.0113$) due to morphological differences in the two NSPs. HR-TEM and XRD established that the PNSP crystallites are of spherical nature and smaller size (45.5 nm) compared to the TNSPs, both favorable characteritics for increased internalisation. Furthermore, FACS flow cytometry confirmed the existence of higher uptake of PNSPs in 9L cells. The ability to be more effectively internalised means a higher proportion of the PNSPs are localised within the cell, making these particles more lethal. It is hypothesised that high LET secondary electrons with very small range, such as Auger electrons, as well as ROS are able to deposit their energy before absorption by the bulk material, delivering single and DSBs to the DNA of the cell. In addition to size and shape, HR-TEM images show the PNSPs to exist with far less aggregation (maximum size of 100 $\mu$m) and increased uniformity. Though the most interesting aspect of these NSPs is shown through the confocal microscope images in figure 6, which demonstrate that both NSPs show a specificity to the cells, forming clusters around the cellular membrane and nucleus. Furthermore, this effect is exasperated at higher concentrations (500 $\mu$g ml$^{-1}$). We establish that the NSPs are congregating around the cells in concentric layers, effectively forming a shell around the cell. The inner layers of this shell generate low energy photoelectrons and Auger electrons, as well as ROS, that create a high LET radiation environment within the shell and lead to effective overkill of the encapsulated cell [37]. The outer layers absorb any secondary electrons originating from within the outer layers themselves since the range of these electrons is less than the thickness of the shell. However, significant localised dose enhancement is induced in cells surrounding the shell through lateral scattering of electrons. Using the 'local effect model' for analysis [38], and considering a cubic volume of interaction surrounding each shelled cell, we see that electrons originating from beam interactions with the media are backscattered off the shell creating a sharp dose peak at the surface of the shell that drops off quickly with increasing distance from the shell. Photoelectons resulting from interactions with the shell may also be forward scattered, creating a similar dose distribution that maximises at the shell surface and drops off quickly towards the edge of the volume of interest. Formation of these shell structures results in a global reduction in the number of individual cells surrounded by the NSP (non-uniform distribution), as well as an increase in the distance between adjacent shell structures.

The difference in SERs for each NP concentration exhibits an unexpected trend, contrary to the literature, where by we note no statistically significant change in the SERs with increasing concentration. Butterworth *et al* [20] established that the degree of radiosensitisation increases with increasing concentration of Au NPs on T98G and AGO-1522B cell lines. The expected increased enhancement is based on the principle that higher concentrations of the NP will increase the number of NP molecules surrounding 9L cells. As a result, higher numbers of secondary

electrons and ROS are generated, culminating in increased damage to the cells. Given the large increase in NP concentration (factor of 10) we would expect a large change in the SER; especially given the 50% increase in the dose enhancement factor (DEF, defined as the ratio of SFs measured at 2 Gy) observed for a factor of 10 increase in Au NP concentration (10–100 $\mu$g ml$^{-1}$) on T98G cells [20]. The lack of additional enhancement at higher NSP concentrations is a direct consequence of the 'shell effect', where by the existence of shells creates a non-uniform distribution of the NSPs among the cells, and increasing the NSP concentration only increases the thickness of the NSP shells, not the number of cells encapsulated by shells. At 150 kVp, the short dose tails result in similar enhancement for both concentrations on both NSPs. Slight increases in enhancement are due to the reduced distance between adjacent shell structures, owing to the increase in shell thickness at higher concentrations.

We see large increases again in radiosensitisation for irradiation of NSPs on 9L cells with 10 MV x-rays. The increase in SER for the TNSPs between 150 kVp and 10 MV is massive, with the high energy part of the spectrum primarily responsible for the improvement in enhancement. The TNSP aggregates still exist here absorbing the lower energy part of the spectrum, however higher energy photoelectrons, Compton scattered electrons and pair-produced electrons also exist here, with particle energies of a few MeVs traveling cms in the bulk material before being absorbed. These long range particles are able to deposit their energy in the cells, however while traversing the bulk material a significant portion will undergo interactions with the NSP aggregate atoms, losing energy and eventually becoming low energy particles with high LET just prior to energy deposition in the cell, giving them enhanced damaging ability. This increase in particle lethality contributes to the linearity observed in the semi-log survival curve. Additionally, scattered electrons originating from interactions with the primary beam exhibit an energy dependent spectrum, where by effective backscattering off TNSP aggregates leads to dose enhancement at the NSP surface propagating radially outwards leading to a 'dose enhancement tail' [14]. These enhancement mechanisms combine to achieve the significant amount of sensitisation observed at 50 $\mu$g ml$^{-1}$.

A proper theoretical analysis of dose distribution at the nanoscale requires Monte Carlo track-structure techniques, simulating interaction-by-interaction the full slowing down of electrons down to the excitation threshold [39]. Furthermore, a theoretical analysis of low-energy electron transport in nanostructures must take into account the reduced dimensionality of the medium (i.e. the nanostructure material), which strongly influences mean free paths, energy loss, penetration ranges, etc [40]. Plasmon decay from the NP should also be considered [41] and be included in theoretical studies and Monte Carlo simulations [42].

Irradiation of PNSPs at 10 MV provides the greatest radiosensitisation of all parameters tested ($SER_{500} = 1.46$, $p = 0.0076$), however similar in magnitude to the TNSPs at this beam energy. This is essentially due to the production of high energy particles, limited not only to photoelectrons (scattered into shelled cells or out of the cells) and Compton scattered electrons, but also pair-produced electrons and positrons [6]. The enhancement effect provided by these particles will be independent of the NSP type, due to the long range associated with their energies, and is uniform throughout the cell culture. Electrons resulting from the low energy region of the photon energy spectrum scattered from the shell will induce overkill damage to the cells, as a result of their high LET [37]. Furthermore, forward and backscattered electrons create radial dose tails, that are a maximum at the shell surface and fall off quickly extending out. These effects combine to produce similar enhancement in the two NSP types, with slightly increased enhancement observed in the PNSPs due to their more dispersed morphology, and more efficient backscattered tail effect. Again, increasing the concentration to 500 $\mu$g ml$^{-1}$ leads to an insignificant change in SER as a result of the 'shell effect', where by the shell thickness increases, leading to similar size dose tails as the 50 $\mu$g ml$^{-1}$ case.

The idea of NSPs forming clusters, or shells, and its effect on the radiosensitisation of radioresistant cells in radiobiological experiments is entirely novel, however, the influence of NP clustering has been considered before in previous Monte Carlo studies. Zygmanski *et al* [43] investigated the effects of NP clustering and changes in particle morhpology on the DER for Au NPs in a water phantom. They were able to show that clusters of NPs produced higher DERs over a greater radial distance (several microns) than single Au NPs (approximately 100 nm), which correlates well with the phenomena observed in this study, and the establishment of a shielding effect, despite the obvious differences in experimental set up. Furthermore, a new study has emerged that conisders the important contribution to dose enhancement from scattered photoelectrons of intermediate energies, rather than just low energy high LET Auger electrons, while also considering the distribution of NPs in the cells, and that the DNA of the nucleus does not need to be the sole target of radiation in achieving effective cell death. This particular study analyses the effects of Au NPs on MDA-MB-231 human breast cancer cells using radiobiological assays and GEANT4 studies, and uses the LEM as well as a biophysical model, to achieve good agreement between simulated and radiobiological results [44], highlighting the need to use models such as these in DERT, and the importance of considering the distribution of the NPs in the cells.

## Conclusion

This study highlights the multiple factors influencing radiosensitisation, and how they may be optimised to maximise the effect with non-toxic ceramic tantalum pentoxide NSPs. The PNSPs were synthesised with spherical shape, smaller particle size and less tendency for aggregation compared to the TNSPs, and yielded a higher SER than the TNSPs at all concentrations and beam energies tested. For both NSPs and all beam energies, the SER demonstrated insignifcant changes in value for varying NSP concentration. However, enhancement was impeded by a shielding mechanism referred to as the 'shell effect'. This effect involves the attraction of the NSPs towards the 9L cells resulting in the formation of layered shells of NSPs around individual cells. The natural affinity of numerous NSPs to be drawn to a particular cell results in a global reduction in the number of cells surrounded by the NSP, and an increase in the distance between adjacent shell structures surrounding their respective cells. Finally, enhancement increased with beam energy, exhibiting a proportional relationship contrary to trends observed in the literature for other NPs, owing to the existence of aggregates in the NSPs. A maximum SER of 1.46 was achieved with irradiation of 500 $\mu$g ml$^{-1}$ PNSPs on 9L cells at a beam energy of 10 MV. This work represents a comparative compilation of the many dependencies dose enhancement relies on, and how they may be optimised for maximum effectiveness. Future experiments will look at more sophisticated production techniques for further optimisation of NSP morphology, while looking at possible functionalisation and combination with other molecules, such as MTX for increased cell death and PEG for improved biocompatibility, eventually culminating in *in vivo* experimentation. Monte Carlo studies are being performed to examine the physical mechanisms underlying the dose enhancement observed here, including investigation into the unexpected shielding mechanism, known as the 'shell effect'. Optimisation of the NSP concentration will be investigated and different cell lines will be probed to look for a differential effect that may further improve DERT.

## Acknowledgments

The authors acknowledge the financial support from the National Health and Medical Research Council (APP1084994). We acknowledge the work done by Dr David Wexler in generating HR-TEM images.

## References

[1] Society A C 2011 *Global Cancer Facts and Figures* 2nd edn (Atlanta: American Cancer Society)
[2] Boyle P and Levin B 2008 *World Cancer Report* (Lyon: International Agency for Research on Cancer)
[3] Khan F M 1994 *The Physics of Radiation Therapy* (Maryland: Williams and Wilkins)
[4] Beauchesne P *et al* 1997 Etoposide sensitivity of radioresistant human glioma cell lines *Cancer Chemother. Pharmacol.* **41** 93–7
[5] Kruse C A, Molleston M C, Parks E P, Schiltz P M, Kleinschmidt-DeMasters B K and Hickey W F 1994 A rat glioma model, CNS-1, with invasive characteristics similar to those of human gliomas: a comparison to 9L gliosarcoma *J. Neuro-Oncol.* **22** 191–200
[6] Alkhatib A, Watanabe Y and Broadhurst J H 2009 The local enhancement of radiation dose from photons of MeV energies obtained by introducing materials of high atomic number into the treatment region *Med. Phys.* **36** 3543–8
[7] Attix F 2004 *Introduction to Radiological Physics and Radiation Dosimetry* (Weinheim: Wiley-VCH)
[8] Sastry K S R 1992 Biological effects of the Auger emitter iodine-125 A review. Report No. 1 of AAPM Nuclear Medicine Task Group No. 6. *Med. Phys.* **19** 1361–70
[9] Tubiana M, Dutreix J and Wambersie A 1990 *Introduction to Radiobiology* (London: Taylor and Francis)
[10] Hainfeld J F, Slatkin D N and Smilowitz H M 2004 The use of gold nanoparticles to enhance radiotherapy in mice *Phys. Med. Biol.* **49** 309–15
[11] Jain S *et al* 2011 Cell-specific radiosensitization by gold nanoparticles at megavoltage radiation energies *Int. J. Radiat. Oncol. Biol. Phys.* **79** 531–9
[12] Tarnuzzer R, Colon J, Patil S and Seal S 2005 Vacancy engineered ceria nanostructures for protection from radiation-induced cellular damage *Nano Lett.* **5** 2573–7
[13] Briggs A *et al* 2013 Cerium oxide nanoparticles: influence of the high-*Z* component revealed on radioresistant 9L cell survival under x-ray irradiation *Nanomedicine* **9** 1098–105
[14] Brown R *et al* 2014 High-*Z* nanostructured ceramics in radiotherapy: first evidence of $Ta_2O_5$-induced dose enhancement on radioresistant cancer cells in an MV photon field *Part. Part. Syst. Charact.* **31** 500–5
[15] Bouchet A *et al* 2014 Characterization of the 9l gliosarcoma implanted in the fischer rat: an orthotopic model for a grade iv brain tumor *Tumor Biol.* **35** 6221–33
[16] Barth R F 1998 Rat brain tumor models in experimental neuro-oncology: the 9L, C6, T9, F98, RG2 (D74), RT-2 and CNS-1 gliomas *J. Neuro-Oncol.* **36** 91–102
[17] Bencokova Z *et al* 2008 Molecular and cellular response of the most extensively used rodent glioma models to radiation and/or cisplatin *J. Neuro-Oncol.* **86** 13–21
[18] Corde S *et al* 2004 Synchrotron radiation-based experimental determination of the optimal energy for cell radiotoxicity enhancement following photoelectric effect on stable iodinated compounds *Br. J. Cancer* **91** 544–51
[19] Ma C M *et al* 2001 AAPM protocol for 40–300 kv x-ray beam dosimetry in radiotherapy and radiobiology *Med. Phys.* **28** 868–93
[20] Butterworth K T *et al* 2010 Evaluation of cytotoxicity and radiation enhancement using 1.9 nm gold particles: potential application for cancer therapy *Nanotechnology* **21** 295101–709
[21] Kominami H *et al* 2001 Solvothermal synthesis of tantalum(v) oxide nanoparticles and their photocatalytic activities in aqueous suspension systems *Phys. Chem. Chem. Phys.* **3** 2697–703
[22] Borchert H *et al* 2005 Determination of nanocrystal sizes: a comparison of TEM, SAXS, and XRD studies of highly monodisperse CoPt 3 particles *Langmuir* **21** 1931–6
[23] Busch W *et al* 2011 Internalisation of engineered nanoparticles into mammalian cells *in vitro*: influence of cell type and particle properties *J Nanopart. Res.* **13** 293–310
[24] Oktaria S 2014 Advances in targeted radiosensitiser and nanotherapeutic agents for cancer therapy *PhD Thesis* School of Physics, Faculty of Engineering and Information Sciences, University of Wollongong
[25] Metcalfe P, Kron T and Hoban P 2007 *The Physics of Radiotherapy, X-rays and Electrons* (Madison, WI: Medical Physics Publishing)

[26] Huang H and Hsieh T 2010 Preparation and characterizations of tantalum pentoxide ($Ta_2O_5$) nanoparticles and UV-curable $Ta_2O_5$-acrylic nanocomposites *J. Appl. Polym. Sci.* **117** 1252–9
[27] Wang X, Zhuang J, Peng Q and Li Y 2005 A general strategy for nanocrystal synthesis *Nature* **437** 121–4
[28] Moffatt W, Pearsall G and Wulff J 1964 *The Structure and Properties of Materials* (New York: Wiley)
[29] Pan Y *et al* 2009 Gold nanoparticles of diameter 1.4 nm trigger necrosis by oxidative stress and mitochondrial damage *Small* **5** 2067–76
[30] Chithrani B D, Ghazani A A and Chan W C W 2006 Determining the size and shape dependence of gold nanoparticle uptake into mammalian cells *Nano Lett.* **6** 662–8
[31] Song Q *et al* 2014 The acute cytotoxicity of bismuth ferrite nanoparticles on PC12 cells *J. Nanopart. Res.* **16** 2408
[32] Mahmoudi M, Simchi A and Imani M 2009 Cytotoxicity of uncoated and polyvinyl alcohol coated superparamagnetic iron oxide nanoparticles *J. Phys. Chem.* C **113** 9573–80
[33] Jain S, Hirst D G and O'Sullivan J M 2012 Gold nanoparticles as novel agents for cancer therapy *Br. J. Radiol.* **85** 101–13
[34] Brunner T J *et al* 2006 *In vitro* cytotoxicity of oxide nanoparticles: comparison to asbestos, silica, and the effect of particle solubility *Environ. Sci. Technol.* **40** 4374–81
[35] Burger N *et al* 2014 A method for the efficient cellular uptake and retention of small modified gold nanoparticles for the radiosensitization of cells *Nanomedicine* **10** 1365–73
[36] McMahon S J *et al* 2011 Biological consequences of nanoscale energy deposition near irradiated heavy atom nanoparticles *Sci. Rep.* **1** 18
[37] McKinnon S *et al* 2016 Study of the effect of ceramic $Ta_2O_5$ nanoparticle distribution on cellular dose enhancement in a kilovoltage photon field *Phys. Medica* **32** 1216–24
[38] Elsasser T and Scholz M 2007 Cluster effects within the local effect model *Radiat. Res.* **167** 319–29
[39] Nikjoo H, Uehara S, Emfietzoglou D and Cucinotta F 2006 Track-structure codes in radiation research *Radiat. Meas.* **41** 1052–74
[40] Kyriakou I, Emfietzoglou D, Garcia-Molina R, Abril I and Kostarelos K 2011 Simple model of bulk and surface excitation effects to inelastic scattering in low-energy electron beam irradiation of multi-walled carbon nanotubes *J. Appl. Phys.* **110** 054304
[41] Werner W S *et al* 2011 Contribution of surface plasmon decay to secondary electron emission from an al surface *Appl. Phys. Lett.* **99** 184102
[42] Emfietzoglou D, Kyriakou I, Garcia-Molina R, Abril I and Kostarelos K 2012 Quasi first-principles Monte Carlo modeling of energy dissipation by low-energy electron beams in multi-walled carbon nanotube materials *Appl. Phys. Lett.* **100** 093113
[43] Zygmanski P *et al* 2013 Dependence of Monte Carlo microdosimetric computations on the simulation geometry of gold nanoparticles *Phys. Med. Biol.* **58** 7961–77
[44] McQuaid H N *et al* 2016 Imaging and radiation effects of gold nanoparticles in tumour cells *Sci. Rep.* **6** 19442